



**HAL**  
open science

# Taking Bragg Coherent Diffraction Imaging to Higher Energies at Fourth Generation Synchrotrons: Nanoscale Characterization

Marie-Ingrid Richard, Isaac Martens, Maxime Dupraz, Jakub Drnec, Veijo Honkimäki, Corentin Chatelier, Clément Atlan, Marta Mirolo, Mor Levi, Eugen Rabkin, et al.

## ► To cite this version:

Marie-Ingrid Richard, Isaac Martens, Maxime Dupraz, Jakub Drnec, Veijo Honkimäki, et al.. Taking Bragg Coherent Diffraction Imaging to Higher Energies at Fourth Generation Synchrotrons: Nanoscale Characterization. ACS Applied Nano Materials, In press, 6 (12), pp.10246-10255. 10.1021/ac-sanm.3c01145 . hal-04125136

**HAL Id: hal-04125136**

**<https://hal.science/hal-04125136>**

Submitted on 12 Jun 2023

**HAL** is a multi-disciplinary open access archive for the deposit and dissemination of scientific research documents, whether they are published or not. The documents may come from teaching and research institutions in France or abroad, or from public or private research centers.

L'archive ouverte pluridisciplinaire **HAL**, est destinée au dépôt et à la diffusion de documents scientifiques de niveau recherche, publiés ou non, émanant des établissements d'enseignement et de recherche français ou étrangers, des laboratoires publics ou privés.

# Taking Bragg Coherent Diffraction Imaging to Higher Energies at Fourth Generation Synchrotrons: Nanoscale Characterization

Marie-Ingrid Richard,<sup>\*,†,‡</sup> Isaac Martens,<sup>‡</sup> Maxime Dupraz,<sup>†,‡</sup> Jakub Drnec,<sup>‡</sup> Veijo Honkimäki,<sup>‡</sup> Corentin Chatelier,<sup>†,‡</sup> Clément Atlan,<sup>†,¶,‡</sup> Marta Mirolo,<sup>‡</sup> Mor Levi,<sup>§</sup> Eugen Rabkin,<sup>§</sup> Joël Eymery,<sup>†</sup> Akshata Naidu,<sup>‡</sup> Tobias U. Schüllli,<sup>‡</sup> and Steven J. Leake<sup>\*,‡</sup>

<sup>†</sup>*Univ. Grenoble Alpes, CEA Grenoble, IRIG, MEM, NRX, 17 avenue des Martyrs,  
F-38000 Grenoble, France*

<sup>‡</sup>*ESRF - The European Synchrotron, 71 Avenue des Martyrs, F-38000 Grenoble, France*

<sup>¶</sup>*Univ. Grenoble Alpes, Univ. Savoie Mont Blanc, CNRS, Grenoble INP, LEPMI, 38000  
Grenoble, France*

<sup>§</sup>*Department of Materials Science and Engineering, Technion-Israel Institute of  
Technology, 3200003, Haifa, Israel*

E-mail: mrichard@esrf.fr; leake@esrf.fr

## Abstract

High-energy Bragg coherent diffraction imaging (BCDI) can enable three-dimensional imaging of atomic structure within individual crystallites in complex environments. Here, we show that sufficient coherent photon flux is available to extend the BCDI technique to higher energies to: 1) obtain improved strain information and sensitivity

at the nanoscale with higher order Bragg reflections, 2) exploit BCDI in embedded materials or complex *operando* environments, 3) reduce x-ray induced sample modification and 4) minimize dynamical scattering effects. We demonstrate the nanoscale imaging technique on the same sub-micron sized crystal at 8.5, 19.9 and 33.4 keV by taking advantage of the brilliance and coherence of the fourth generation Extremely Brilliant Source of the ID01 beamline at ESRF - The European Synchrotron (Grenoble, France). The photon flux, data quality, resolution and strain information are compared. We also show first coherent diffraction measurements performed at the ID31-EBS beamline at an energy of 41 keV.

## Keywords

high-energy, Bragg coherent diffraction imaging, nanostructures, strain, morphology, diffraction

## Introduction

Coherent diffraction imaging (CDI) exploits the inherent coherence of a light source to image materials with a resolution limited fundamentally by the wavelength of the light, but in practice by the extent of the scattering (typically limiting spatial resolution to 10 nm or less). In the case of crystalline materials and an x-ray wavelength light source, Bragg peaks are readily accessible. Bragg CDI (BCDI) provides an additional contrast mechanism, the local symmetry of the Bragg peak can be broken, giving rise to a complex three-dimensional (3D) image. The amplitude of the reconstructed complex image corresponds to electron density which scatters to the Bragg peak, the so called "Bragg electron density", and the phase corresponds to the deviation of a perfect crystalline lattice away from its reference, the Bragg peak itself. Thus in addition to a high spatial resolution a strain resolution down to  $10^{-4}$  is achieved.<sup>1-3</sup>

The first BCDI experiments of individual microstructures were made possible with the advent of highly stable optics preserving the coherence of x-ray beams at third generation synchrotron sources.<sup>4</sup> In that case an harmonic rejecting mirror and a double crystal monochromator were combined with an aperture that was placed at some distance from the source to select a coherent portion of the beam which was used to illuminate the sample. Since the first demonstration, microstructures have become nanostructures and simple characterisation has evolved to complex *operando/in situ* measurements. The principal optical components have remained the same, and are kept to a minimum to reduce the impact on the coherence of the beam, but the improvement of focusing optics, placed after the aperture, have led to smaller and smaller beams providing the flux densities required to routinely image few hundred nanometer sized crystals in the 7-13 keV energy range.<sup>5</sup> This method now plays a significant role in materials science, physics, chemistry and engineering. The technique has been recently applied *in situ* for instance during high-pressure,<sup>6</sup> catalytic<sup>7-9</sup> or battery<sup>10,11</sup> experiments.

The coherence of the x-ray beam is described by transverse (2D) and longitudinal components relative to the beam propagation, the volume of which defines the limit of the size of the object that can be imaged. The transverse coherence lengths, the eventual aperture of the focusing optics, are determined by the source size<sup>12</sup> and are typically tens to hundreds of microns. The longitudinal coherence however is defined by the bandwidth of the x-ray beam, set by the monochromator. For a typical (111) silicon crystal of bandwidth  $10^{-4}$ , it is less than a micron.<sup>13</sup> Note that the maximum sample size limit due to longitudinal coherence also depends on the scattering geometry. Thus focusing optics and monochromators are optimised to produce focal spots and longitudinal coherence lengths that match (assuming an approximately spherical sample) while optimising flux density on the sample.

The realisation of fourth generation sources<sup>14,15</sup> has improved the available flux densities at typical operating energies and extended the energy range at which sufficient coherent flux can be delivered to the sample beyond 40 keV. Improvements in the emittance properties

of x-ray sources intrinsically lead to more coherent photons, the consequences of which are discussed further by Singer *et al.*<sup>16</sup> The realisation of the multi-bend achromat lattices in storage rings (Max IV<sup>15</sup> and ESRF-EBS<sup>14</sup>) provide emittance properties which improve the available coherent flux by up to several orders of magnitude, in the latter case sufficient coherent photons are available at higher x-ray energies for BCDI measurements.<sup>17,18</sup> Taking the ID01 beamline at the ESRF-EBS (used in this study) as an example, the source size has decreased by approximately a factor 2, and the beam divergence a factor 14 (particularly in the horizontal direction, from 170  $\mu\text{rad}$  (old ESRF) to 14  $\mu\text{rad}$  (ESRF-EBS)), leading to a total gain of 28 in coherent flux. However for certain experiments, such as nanometric sized crystals one could remove the optics (monochromator) as the bandwidth would now be small enough to satisfy the longitudinal coherence and delivers an additional factor 5-10.

As shown in Figure 1 (a), moving to higher energy x-rays can reduce the available flux by several orders of magnitude, the principle advantage is deeper penetration through sample environments. This permits more realistic *in situ* experiments, and reduces beam damage. The hunt for resolution leads to incredible flux densities, and radiation induced modification of samples is somewhat inevitable.<sup>19-21</sup> Radiation damage is generally proportional to the absorbed dose. This dose results from photoelectric absorption of x-rays with the concomitant emission of a photoelectron and either an Auger electron or a fluorescent x-ray, and to a minor extent, x-ray energy loss due to Compton (inelastic) scattering. The ratio of the scattering cross section to absorption (photoelectric) cross-section is therefore a convenient metric for the dose-damage efficiency. Figure 1 (b) plots the dose-damage efficiency for Pt atoms, which improves at high energies above absorption edges. This effect is even more pronounced for lighter elements (*e.g.* battery materials), where absorption edges lie below 10 keV, in addition to any absorption by the sample environment. Recently, beam damage has been investigated during *operando* powder x-ray diffraction synchrotron experiments of battery materials.<sup>22</sup> This work reveals that beam damage depends strongly both on x-ray energy, amount of exposure and on the cell chemistry, *i.e.* the chemical composition of

the electrode. In general a higher dose and lower x-ray energies results in increased beam damage.

Moving to higher x-ray energies offers several additional advantages. A larger portion of reciprocal space and Bragg peaks can be accessed, which are advantageous due to their enhanced structural sensitivity.<sup>23</sup> High-energy x-rays decrease background noise on the detector, due to less scattering of x-rays from air in the beam path. At high energies, refraction and absorption become less significant and have a diminished impact on BCDI reconstruction.<sup>24</sup> In addition, it is easier to align samples and measure multiple Bragg peaks (to retrieve the strain tensor), but leads to an increase in requirements for the sample goniometers as Bragg peaks are even sharper.<sup>25,26</sup> It is important to note that high-order Bragg peaks are difficult or impossible to access at lower beam energies, as the beam energy is inversely proportional to the Bragg angle,  $\theta_{Bragg}$ . As an example, the Bragg angle of the **402** Pt reflection is  $56.24^\circ$  at 8.5 keV and  $12.22^\circ$  (4.6 times smaller) at 33.4 keV. While the Bragg angle of the **533** Pt reflection is  $18.07^\circ$  at 33.4 keV, the **533** Pt reflection is unreachable at 8.5 keV. For a particle size of 500 nm, the detector (supposing a detector with a 55  $\mu\text{m}$  pixel pitch) should be positioned at a minimum distance of 0.37 m at 8.5 keV and 1.48 m at 33.4 keV for an oversampling in the detector plane larger than 2 (*i.e.*, 2 pixels per fringe, the Nyquist limit). This implies that a longer sample-to-detector distance is necessary at high energy to ensure diffraction pattern oversampling, due to compression of reciprocal space. Emerging strategies capable of reconstructing three-dimensional strained crystallites from undersampled Bragg diffraction datasets, such as pixel-area integration<sup>27</sup> may relax this requirement.

Moving to higher energies also presents several challenges, the compression of reciprocal space and the need to oversample the diffraction pattern in order to retrieve an image requires small pixels and high Z sensor material, large sample to detector distances, and precise sample manipulation (rotation  $< 10^{-3}$  degrees). Integration of high quality GaAs and CdTe sensors in hybrid photon counting pixel detectors now provides single photon sensitivity at high energies and has already proven successful for CDI measurements,<sup>28-30</sup>

after flatfield correction.

Recently, high-energy BCDI has been demonstrated on individual crystalline domains in a poly-grain material by exploiting the partial coherence of a high-energy x-ray beam (52 keV)<sup>31</sup> at a third-generation synchrotron light source. The lattice displacement was obtained with an approximate spatial resolution of 47.5 nm on a few hundred nanometer crystal, with an exposure time of 600 sec per frame. Here we demonstrate the application of Bragg coherent imaging at a high energy (33.4 keV) using the coherent beam of the fourth generation Extremely Brilliant Source of the ID01 beamline of the European Synchrotron (ESRF-EBS, Grenoble, France). The exposure time per frame was 1 sec leading to a spatial resolution of  $\sim 17$  nm. We compare the Bragg coherent imaging measurements as well as reconstructed electron density, phase and strain fields of an identical Pt nanocrystal at low (8.5 keV), medium (19.9 keV) and high (33.4 keV) energies. The chosen energies correspond to the maximum flux available (minimum undulator gap) for the 1<sup>st</sup>, 3<sup>rd</sup> and 5<sup>th</sup> harmonics of the 27 mm period undulators at the ID01-EBS beamline (see Figure 1(a)). Variations in the reconstructed phase show significant deviations in the structure between measurements and can be understood as due to both carbon contamination, as confirmed by scanning electron microscopy or beam damage. We also show the first coherent diffraction measurements performed at the ID31-EBS beamline at an energy of 41 keV and discuss the associated practical limitations. High energy BCDI opens up a new class of experiments for three-dimensional *in situ* and *operando* high-resolution strain field mapping in complex environments (for instance; photo-electro-catalytic, battery or diamond cell) and of multi-functional materials.

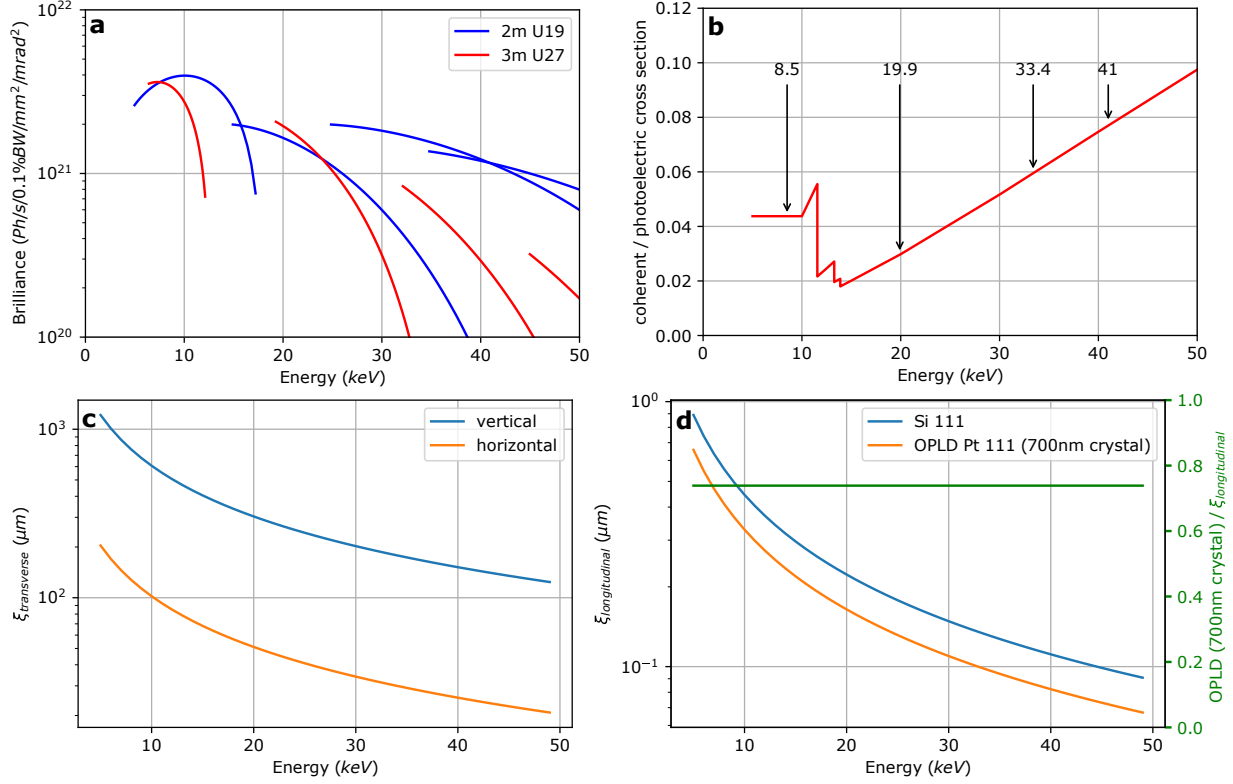


Figure 1: **X-ray characteristics.** (a) Evolution of the brilliance as a function of energy for a 3m long U27 and an in vacuum 2m long U19 insertion devices. (b) Ratio of the scattering cross-section to absorption (photoelectric) cross-section of Pt atoms as a function of energy. (c) Transverse and (d) longitudinal coherence lengths as well as the optical path length difference (OPLD) at the **111** reflection of a 700-nm Pt crystal as a function of energies at the ID01-EBS beamline.

## Results

### Coherence lengths and expected flux

The coherence properties of the beam are paramount for a successful BCDI experiment. Based on theoretical source parameters, a full width at half maximum (fwhm) size of the photon beam of 12 μm (vertical) x 72 μm (horizontal) was expected, and was verified by imaging the source itself at ID01-EBS. The corresponding transverse coherence lengths<sup>12</sup> across the full energy spectrum of the ID01-EBS beamline are shown in Figure 1(c). The ξ<sub>transverse</sub> at 8.5, 19.9 and 33.4 keV is 120 μm x 716 μm, 51 μm x 304 μm and 30 μm x 181 μm (horizontal x vertical), respectively. At constant flux density this would lead to a decrease of

available coherent flux with  $1/E^2$ . As the angular flux density is not constant as a function of energy, a further decrease of available coherent flux occurs in the energy regime above the diffraction limit leading to a further scaling of the coherent flux with the source brilliance. As this last parameter is dependent on the available insertion device technology, its decrease as a function of x-ray energy is shown in Figure 1(a). As discussed earlier, the longitudinal coherence will provide the limit to sample dimension, hence the beam is condensed with focusing optics to an equivalent size in the transverse directions to improve flux density. The ability to tune the longitudinal coherence is limited on most beamlines, as it is set by the bandwidth of the monochromator, in this case we used a Si 111 monochromator to deliver the most photon flux to the sample which sets a limit on the crystal size of  $\sim 700$  nm. It is important to note that the useful longitudinal coherent illumination is coupled to the chosen Bragg reflection for the BCDI measurement, the optical path length difference (OPLD) between two x-rays passing through the extremes of the sample depends on the projection of the crystal shape onto the Q-vector and is subsequently relaxed at higher energies, lower Bragg angles, allowing slightly larger crystals to be measured,<sup>13</sup> as demonstrated by the ratio of longitudinal coherence to that of Platinum **111** reflection being constant, see Figure 1(d). However it is important to take it into consideration when using high energies to access higher order Bragg peaks. In Platinum at 33.4 keV the **533** reflection requires 4 times greater longitudinal coherence length than the **111** reflection.

At ID01-EBS, the anticipated coherent flux at 8.5, 19.9 and 33.4 keV is  $3 \times 10^{11}$ ,  $4 \times 10^{10}$  and  $1.5 \times 10^{10}$  ph/s, before losses due to focusing and eventual measurement are considered.

## **Bragg coherent diffraction at three energies**

The sample consisted of Pt nanocrystals (NCs), which were prepared by the solid-state dewetting of a 30-nm thin Pt film for 24 hours at 1100°C in air on yttria-stabilised zirconia (YSZ) (see Figure 2 and Experimental Section). To ensure to measure the same particle at different energies, the sample has been patterned, and the location of the measured particle

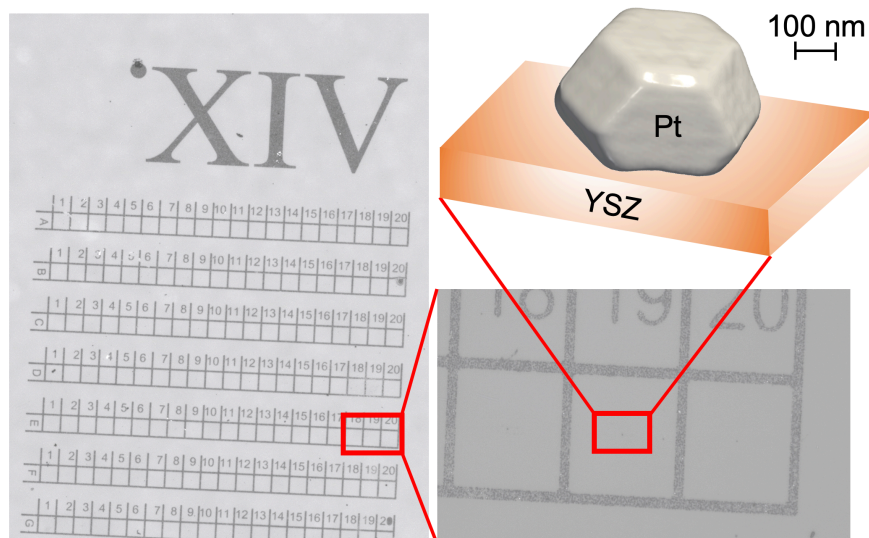


Figure 2: **Scheme of the synthesis.** The faceted Pt particles have been obtained by solid-state dewetting on yttria-stabilised zirconia (YSZ). The sample has been patterned by a standard photolithography method to facilitate the location of the Pt particles.

is precisely defined. The position of both the particle and the beam can be accurately determined using an optical microscope. Furthermore, the x-ray beam can be observed through the microscope due to the fluorescence of the sapphire substrate. Bragg coherent diffraction imaging measurements were performed on the same Pt particle at the ID01 nanodiffraction beamline (core energy regime from 6 to 40 keV) at the Extremely Brilliant Source (EBS) of ESRF. BCDI was employed to retrieve the shape and the projected three-dimensional displacement and strain field within a single Pt NC. Three energies have been selected: 8.5 keV (standard), 19.9 keV (medium) and 33.4 keV (high energy). For all energies, the beam has been focused using Beryllium compound refractive lenses. The number of lenses required is energy dependent and was adapted to accommodate both; the beam size (numerical aperture of the optic) and the maximum coherent flux density.

In a typical BCDI measurement, a coherently illuminated single crystal is rotated through the Bragg condition in small angular steps (typically  $0.005^\circ$  ( $0.0033^\circ$ ) over a  $1.6^\circ$  ( $1^\circ$ ) range for a 8.5 keV (33.4 keV) energy beam) to get a three-dimensional diffraction pattern (see

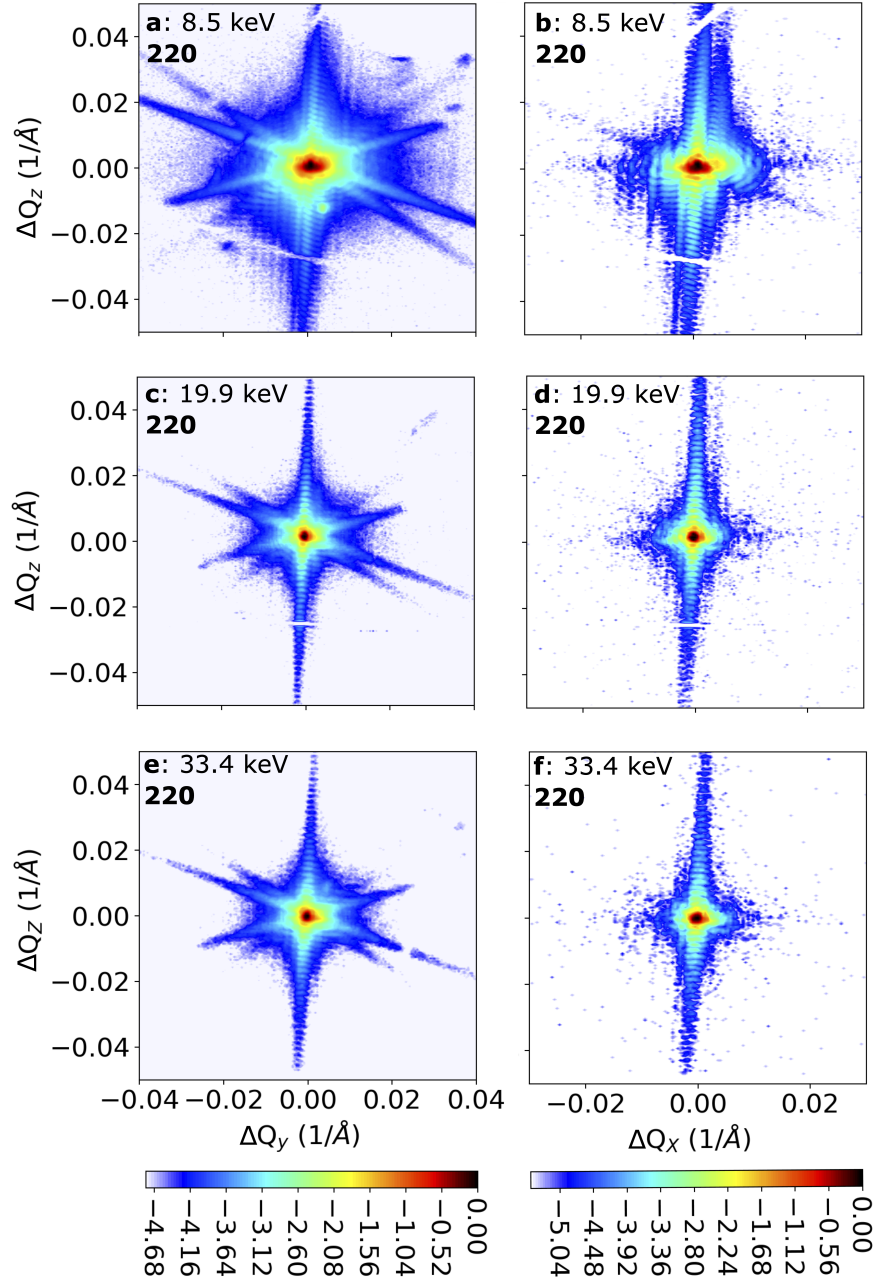


Figure 3: **Coherent diffraction patterns.** (a)-(c)-(e). Integrated diffraction patterns along the  $Q_x$  (x-ray beam) direction for the same particle measured at three energies. (b)-(d)-(f)  $\Delta Q_x - \Delta Q_z$  slices of the measured intensity for the same particle at three energies at the maximum of the rocking-curve. The data, which have been measured at the **220** Bragg reflection, is displayed in logarithmic scale and are normalised by the maximum measured intensity.

Figure 3). The size of the angular steps used in the measurement is significantly larger than the smallest step size of the rotation axis employed ( $0.0000152^\circ$ ). A two-dimensional GaAs

MAXIPIX detector<sup>30</sup> has been used to collect the BCDI data at medium and high energies, whereas a Si MAXIPIX detector has been used for BCDI measurements at the standard energy. The asymmetric **220** Bragg reflection has been measured at the three energies. This reflection is sensitive to local lattice displacement and strain variations along the [110] direction, the measured particle being [111]-oriented relative to the substrate normal (*i.e.* its *c*-axis being oriented along the [111] direction).

### Retrieved local lattice displacement and strain

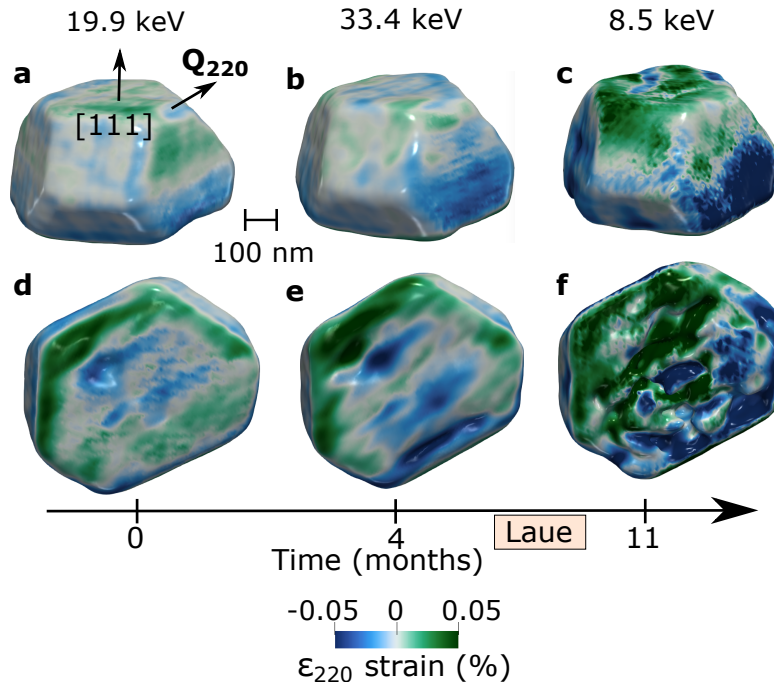


Figure 4:  $\epsilon_{220}$  **strain**. Evolution of the strain along the [220] direction of the Pt particle recovered from Bragg coherent diffraction imaging measurements at 19.9 keV (a, d), 33.4 keV (b, e) and 8.5 keV (c, f). The top (bottom) row shows a side (bottom) three-dimensional view of the particle. The reconstructed electron density of the Pt particle is drawn at 30% (50%) at 8.5 keV (at 19.9 keV and 33.4 keV) of the maximum electron density. The isosurface value of the electron density (coloured with the retrieved  $\epsilon_{220}$  strain) has been chosen based on the criterion described in Ref.<sup>32</sup> The chronology of the measurements is displayed on the x axis, highlighting when Laue measurements were made.

Figure 4 displays the retrieved strain,  $\epsilon_{220}$ , spatial derivative of the retrieved displacement along the [220] direction of the measured Pt particle at the three energies. The data have

been collected in air first at 19.9 keV (in May 2021), then at 33.4 keV (September 2021) and finally at 8.5 keV (April 2022). In-between the BCDI data collections at 33.4 keV and 8.5 keV Laue measurements (energy range between 5 and 25 keV) have been performed in air. Phase retrieval algorithms were used to invert the three-dimensional data from the reciprocal space (see Figure 3 which displays the associated coherent diffraction patterns) into real space. The same series of algorithms has been applied for the three energies. The reconstructed Bragg electron density and phase were obtained using the PyNX python package.<sup>33</sup> *Gwaihir*, a user-friendly and open-source Jupyter notebook graphical user interface, was used to process and analyse the Bragg coherent X-ray diffraction data.<sup>34</sup> The phase corresponds to the projection of the displacement field onto the scattering vector (here,  $\mathbf{Q}_{220}$ ). The retrieved phase is then processed to establish the maps of displacement and strain within the single NC using the BCDI python package.<sup>35</sup> The measurement of a single Bragg peak only provides a single component of the strain tensor. As we measure the **220** Bragg reflection, the reconstructed phase in 3D only encodes the lattice displacement along the [110] direction, which implies that the derived displacement field (here, the strain inside the (220) planes),  $\varepsilon_{220} = \frac{\partial u_{220}}{\partial x_{220}}$ , is a projection along the [110] direction of the actual full strain field. Slices of the reconstructed electron density at 19.9 keV as well as slices of the reconstructed phase from the asymmetric **220** Bragg reflection for the three energies are shown in Figure 5. Spatial resolution was quantified by differentiating line profiles of electron density amplitude across the object-air interface and by fitting these profiles with a Gaussian function. The average 3D spatial resolution, taken as  $2\sigma$  of the fitted Gaussian, corresponds to 22 nm at 8.5 keV, 15.5 nm at 19.9 keV and 16.8 nm (see Supplementary Figure 1) at 33.4 keV. The measurement time was 6 min 14 sec, 13 min 24 sec and 25 min 50 sec at 8.5 keV, 19.9 keV and 33.4 keV, respectively.

As mentioned above, Figure 3 displays the three-dimensional data measured at the **220** Bragg reflection for the different energies. The maximum intensity is  $1.5 \times 10^5$ ,  $1.79 \times 10^5$  and  $1.27 \times 10^5$  counts/sec at 8.5, 19.9 and 33.4 keV, respectively. The two-dimensional MAXIPIX detector is non-linear above about  $1.5 \times 10^5$  counts/sec. For all the measurements, we adapt

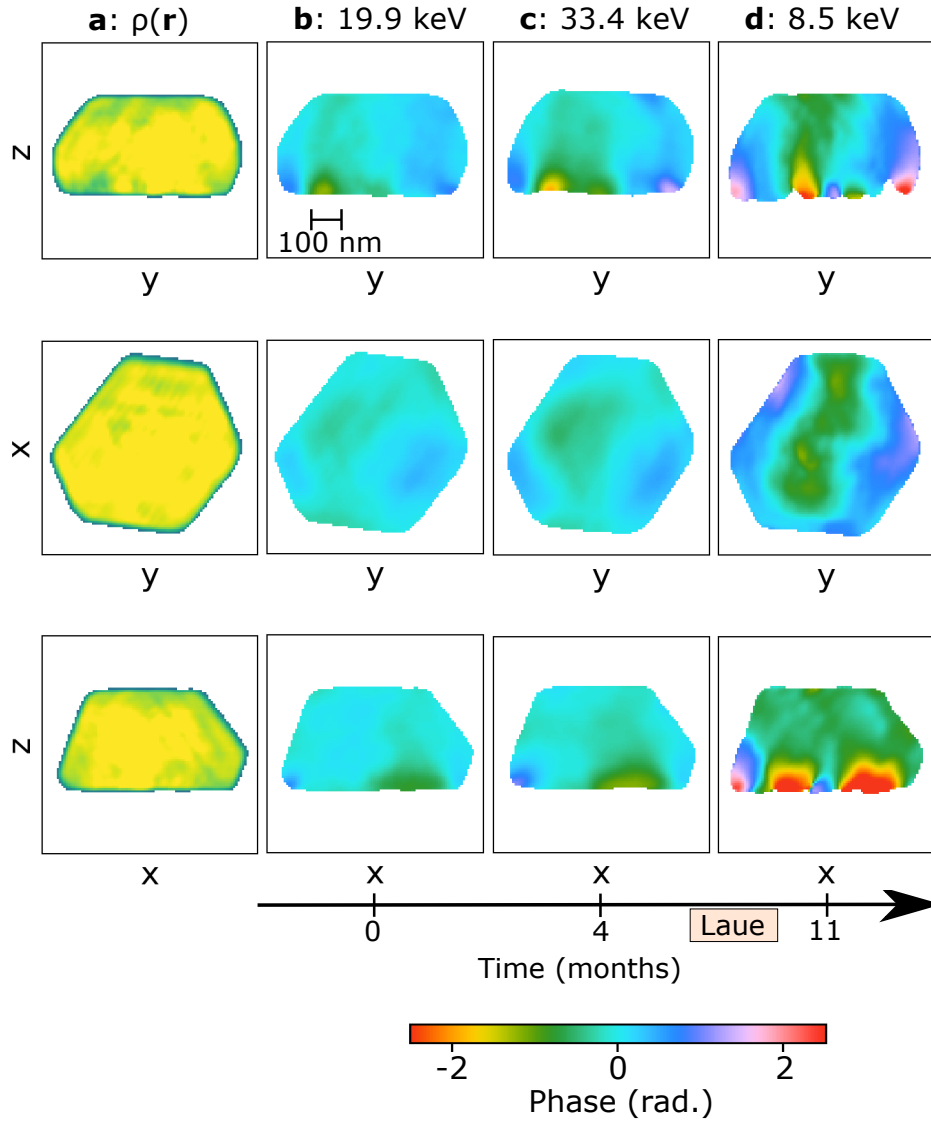


Figure 5: **Slices of the reconstructed Pt particle.** (a) Reconstructed electron density. (b)-(d) Slices at the middle of the Pt particle of the phase retrieved at the asymmetric **220** Bragg reflection for the three different energies and as a function of time.

the coherence slits so that the maximum counts measured on the detector is close to the non-linearity of the pixel detector. Two additional filters were necessary to collect the data at 8.5 keV.

## Discussion

As demonstrated in Figures 3 and 4, the upgraded Extremely Brilliant Source of the European Synchrotron enabled the measurement of the Bragg coherent diffraction pattern of a NC at 33.4 keV at the ID01 beamline of ESRF. After applying phase retrieval algorithms, the same morphology (faceting) of the NC is observed for the three energies. A similar spatial resolution is obtained for the three energies, as we have adapted the size of the coherence slits and adjusted the number of filters/absorbers (two at 8.5 keV and zero for the other cases) before the sample to get a similar maximum intensity (hence similar integrated intensity) onto the detector for the three energies. A much better spatial resolution (5-10 nm) could have been obtained for the dataset measured at 8.5 keV, if the two filters would have been removed. The same electron density is observed for the three energies, however, a different retrieved phase (Figure 5) and strain (here,  $\varepsilon_{220}$  component, see Figure 4) are observed inside the NC. Note that the measurements have been done several months apart. An increase of the heterogeneity and magnitude of the strain is observed as a function of time. Weak variations are observed between the measurements at 19.9 keV and 33.4 keV, whereas large variations are observed between the measurements at 33.4 keV and 8.5 keV, where in-between the BCDI data collections both Laue measurements (energy range between 5 and 25 keV) and BCDI on other reflections were performed, we estimate at least 24 hours of x-ray exposure. A clear change of the diffraction pattern is observed at 8.5 keV (see Figure 3(b)), where an extra streak is visible perpendicular to the  $Q_x$  direction, within the  $Q_x$ - $Q_z$  plane, which may indicate potential formation of defects. We observed strong variations of the phase (see Figure 5 and Supplementary Figure 2) and strain at the NC/substrate interface at 8.5 keV. This is the signature of the formation or evolution of a dislocation network at the particle interface with the substrate. Note that all the measurements have been performed in air for this test sample, where nano-focused x-rays can induce the formation of a C-contamination layer.<sup>36</sup> Figure 6 shows two scanning electron microscopy images of the measured Pt particle at an electron energy of 3 kV and 26 kV, respectively. At low kV, an

inhomogeneous layer is observed on top of the Pt particle. This layer has a low Z-density as this layer is no longer visible at higher energy. This contamination can be caused by photoelectron emission from the NC, leading to cracking of remaining hydrocarbons from air.<sup>37</sup> The shell could have grown inhomogeneously with internal stress, leading to inhomogeneous strain inside the particle. The formation of the layer may result from a cumulative dose effect with time. The contamination may have also been induced by ozone formation during x-ray irradiation in air. Measurements in inert atmosphere or vacuum will be necessary to avoid contamination or identify the source of such sample modification.

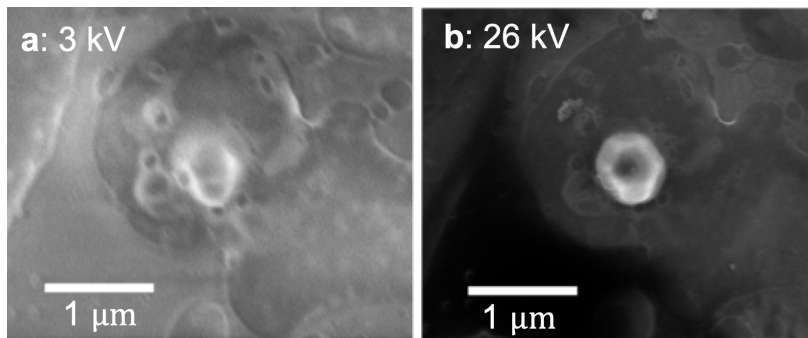


Figure 6: **Contamination.** Scanning electron microscopy image of the Pt particle after Bragg coherent diffraction imaging in air measured at an electron energy of 3 kV (a) and 26 kV (b). The scale bar corresponds to 1  $\mu\text{m}$ .

At 19.9 keV, the  $\bar{5}\bar{3}\bar{3}$  Pt reflection has been measured. This reflection is unreachable at 8.5 keV. Figure 7 displays slices of the reconstructed particle (its phase  $\phi_{\bar{5}\bar{3}\bar{3}}$ , lattice displacement,  $u_{\bar{5}\bar{3}\bar{3}}$  and strain,  $\varepsilon_{\bar{5}\bar{3}\bar{3}}$ ) at this asymmetric Bragg reflection. These results can be compared with the phase ( $\phi_{220}$ ), the lattice displacement ( $u_{220}$ ) and strain ( $\varepsilon_{220}$ ) recovered at the  $220$  Pt Bragg reflection. Note that to allow easier convergence of the phase retrieval algorithms, the support retrieved from the  $220$  Pt reflection has been used for the data measured at the  $\bar{5}\bar{3}\bar{3}$  Pt reflection. As expected, the retrieved phase is larger at the  $\bar{5}\bar{3}\bar{3}$  Pt reflection. At higher index reflection, we are more sensitive to strain variations as smaller  $d$ -spacings are probed.

The same sample, but different crystal of similar dimension, has also been measured at the ID31 beamline of EBS-ESRF at a higher energy of 41 keV (see Experimental Section).

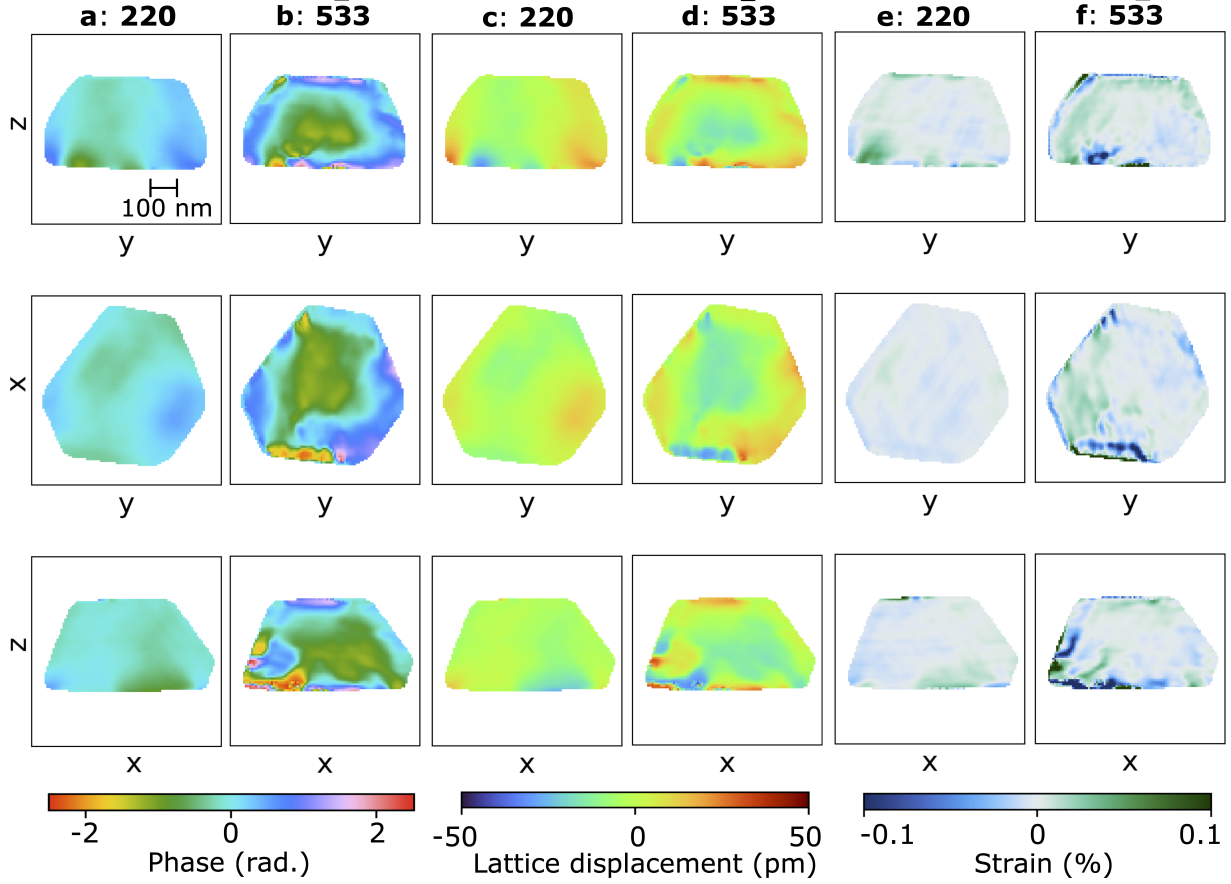


Figure 7: **Comparison between low- and high-index reflections at 19.9 keV.** Retrieved phase, lattice displacement and strain for the (a, c and e) **200** and (b, d and f)  **$\bar{5}\bar{3}\bar{3}$**  Pt reflections.

ID31 is dedicated to interface and materials processing studies using high energy x-rays. Note that the slits (Tungsten slits with a depth of 6 cm) are not optimised for coherent diffraction. Figure 8(c) displays the 3D diffraction pattern of the  $\bar{1}\bar{1}1$  diffraction of a single Pt particle (measurement duration of 4 min, counting time of 1 sec/point with 200 points over  $0.5^\circ$ ). The maximum intensity is 81800 counts/sec. Thickness fringes are well observed along some streaks. The signature of any truncated (faceted) crystal produces a crystal truncation rod, which corresponds to a streak of intensity in reciprocal space normal to the surface. Thickness fringes validate the coherence of the beam along these directions. The interference fringes are a sensitive probe of the size of the investigated particle. Supposing that the particles are not or weakly deformed, the distance between fringes is inversely proportional to the

particle's height. The particle has a diameter of 600 nm. Figures 8(a, b, d and e) display central frames along different directions of the crystal and its associated reconstructed phase along the  $[\bar{1}11]$  direction. The finite shape of the particle is well reconstructed as well as the phase variation (proportional to lattice displacement along the  $[\bar{1}11]$  direction) inside the crystal despite that the fringes are not well resolved in the horizontal plane as the detector has been positioned at the limit of oversampling.

When performing BCDI measurements at high energy, one major limitation is the need for a long sample-to-detector distance to ensure sufficient diffraction pattern oversampling. For example, to achieve an oversampling of 3 with a  $55 \mu\text{m}^2$  pixel size detector at 80 keV, a detector distance of at least 10.64 m is required. However, the required detector distance can be reduced by using a detector with a smaller pixel size. For instance, a  $10 \mu\text{m}^2$  pixel size detector placed only 2 m from the sample would be sufficient to measure a 1  $\mu\text{m}$ -particle at 80 keV. An alternative could be to exploit sub-pixel translations of the detector or up-sampling<sup>27,38,39</sup> could be employed to overcome the issue of the required detector distance. The available rotation stage (a small step size of  $0.0000152^\circ$  at ID01-ESRF) is not a limitation for high energy measurements. Compound refractive lenses provide high quality beams and are very efficient at high energies. In addition, better focusing optics and continuous improvement of beamline optics can increase the coherent flux on the sample, which may help to mitigate the challenge of smaller coherence lengths at high energy. By implementing these strategies, it will be possible to obtain high-quality BCDI measurements even at higher energies.

## Conclusion

We have demonstrated BCDI at a high energy of 33.4 keV and at the nanoscale by taking advantage of the fourth generation Extremely Brilliant Source of the European Synchrotron. We obtained a similar quality for the reconstructions at 8.5, 19.9 and 33.4 keV for on average

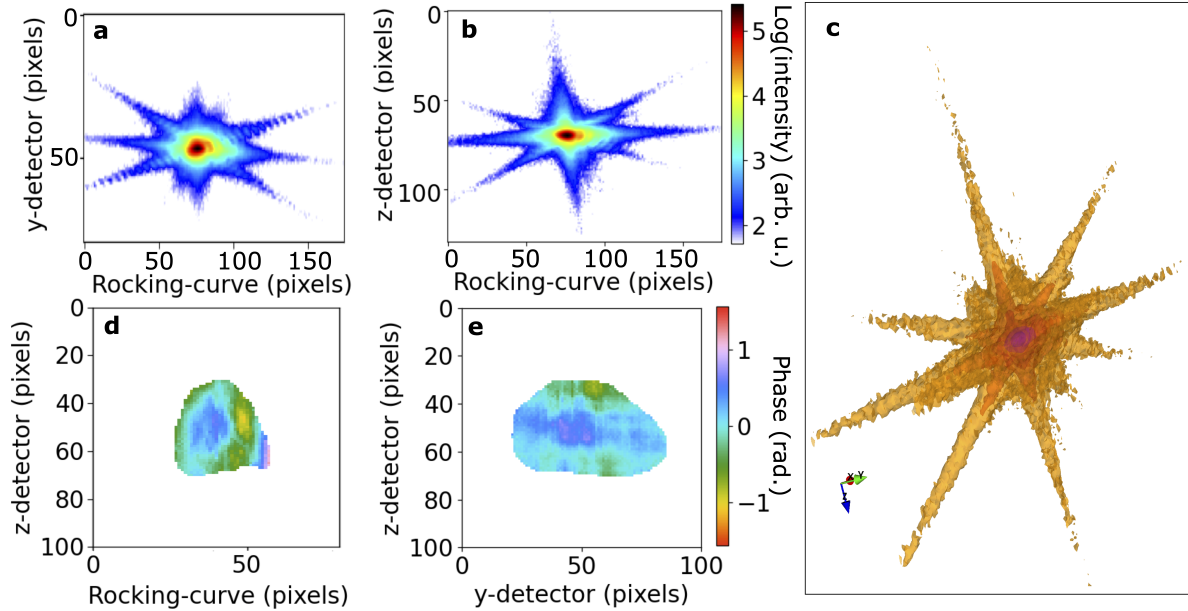


Figure 8: **Bragg coherent diffraction imaging at the ID31-EBS beamline.** BCDI measurement of a single Pt particle at 41 keV. Sum of the 3D intensity (a) along the rocking-curve and out-of-plane  $z$  detector directions and (b) along the rocking-curve and in-plane  $y$  detector directions. (c) 3D diffraction pattern in the detector frame. (d)-(e) Central frames along different directions of the reconstructed crystal and associated phase.

the same measured maximum intensity. Special care should be taken during the measurements to avoid sample damage like carbon contamination by doing measurements under vacuum or inert gas. In the near future, Bragg coherent diffraction experiments at 20-40 keV energies will mitigate sample damage during *in situ* and *operando* measurements as high-energy x-rays interact weakly: less absorption and generated photoelectrons can be ejected rather than reabsorbed. This will also allow to measure embedded crystals in complex or difficult-to-access environments that require the long penetration depths of high-energy x-rays.

## Experimental

**Sample preparation.** The Pt film was deposited on yttria-stabilised zirconia (YSZ) with an electron beam evaporator. The Pt nanocrystals have their  $c$ -axis oriented along the [111]

direction normal to the (001) YSZ substrate. A standard photolithography method was employed to prepare a patterned layer of photoresist on YSZ prior to the electron beam evaporation of Pt. The lithographic processing route ensured that a number of dewetted Pt particles are well-separated from their neighbors and that only one crystallite is irradiated by the incoming x-ray beam. The diameter of the particles ranges between 200 nm and 600 nm.

**Diffraction setup detail at ID01-ESRF.** The sample was mounted on a  $(x,y,z)$  scanning piezoelectric stage. The scanning stage has a stroke of 100  $\mu\text{m}$  along  $x$  and  $y$  with an encoder resolution of about 1 nm. The detector has been positioned at a distance of 0.7288 m, 1.68 m and 2.2 m from the sample at 8.5 keV, 19.9 keV and 33.4 keV.

**Diffraction setup detail at ID31-ESRF.** The 3<sup>rd</sup> harmonic of a 2m long U14 undulator was selected. A 1m long Ar gas absorber (330 mbar) with two diamond screens (thickness 300  $\mu\text{m}$ ) reduced the heat load on the monochromator. A multilayer monochromator (NiV/B4C multilayer with 500 periods and 1.98 nm spacing) reduced the bandwidth to  $3.2 \times 10^{-3}$ . After the multilayer monochromator, a Si(511) channel cut monochromator has been installed. Then, a transfocator consisting of 19 aluminium lenses was located 9 m from the sample and 110 m from the source (radius at the apex and the geometrical aperture of the lenses are 200  $\mu\text{m}$  and 900  $\mu\text{m}$  respectively) focused the beam to the end station. A set of high power slits (50  $\mu\text{m}$  (horizontally) x 300  $\mu\text{m}$  (vertically)) were used to select the coherent portion of the beam at a distance of 100 m from the source. The measured beam size at the sample position was 10 x 10  $\mu\text{m}^2$  (vertical x horizontal). The sample was mounted on a stack of Smaract piezo motors, a single rotation stage, with two linear  $(x, y)$  translations on top, which move in the plane perpendicular to the rotation axis. It was translated to the beam position using a Huber stack and tilted by  $0.5^\circ$  to illuminate a large number of crystals. An optical microscope was positioned above the sample to confirm beam and rotation axis coincidence, with a GaP fluorescent screen. A 2D 2M Pilatus detector with a pixel size of

172  $\mu\text{m}^2$  (1475 pixels  $\times$  1679 pixels) was first positioned close (few tens of centimetres) to the sample to detect the powder diffraction rings of the illuminated Pt particles. A Pt wire was used to calibrate the detector distance and to ensure that the observed rings were from Pt. The detector was then positioned at 6.25 m from the sample to zoom in, *i.e.* oversample, on the  $\bar{1}11$  diffraction reflection of single Pt particles. At this distance, an oversampling of 2 (*i.e.* 2 pixels per fringes, the Nyquist limit) in the detector plane corresponds to a particle size of 550 nm.

**Phase retrieval.** Phase retrieval was carried out on the raw diffracted intensity data. The initial support, which is the constraint in direct space, was estimated from the auto-correlation of the diffraction intensity. A series of 1000 Relaxed Averaged Alternating Reflections (RAAR<sup>40</sup>), plus a series of 50 Hybrid Input Output (HIO<sup>41–43</sup>) followed by 800 Error-Reduction (ER<sup>44,45</sup>) steps, including shrink wrap algorithm every 50 iterations,<sup>46</sup> were used. The phasing process included a partial coherence algorithm to account for the partially incoherent incoming wave front.<sup>47</sup> To ensure the best reconstruction possible, we kept only the best 5 reconstructions (with lowest free Log-Likelihood<sup>48</sup>) from 30 with random phase start and performed the decomposition into modes.<sup>48</sup> The reconstruction was then corrected for refraction and absorption using the *bcdi* package.<sup>35</sup> After removing the phase ramp and phase offset, the data was finally interpolated onto an orthogonal grid for ease of visualisation.

## Acknowledgement

We thank ID01-ESRF beamline staff for excellent support during the experiment. This project has received funding from the European Research Council (ERC) under the European Union’s Horizon 2020 research and innovation programme (grant agreement No. 818823). We also wish to thank the support by a grant from the Ministry of Science and Technology, Israel and from the Centre National de la Recherche Scientifique (CNRS), France. A. Naidu

wants to acknowledge the NSF PIRE Award # 1545884 and the PennAbroad program for the opportunity of the internship.

## Supporting Information Available

Evaluation of the spatial resolution and three-dimensional retrieved phase

## References

- (1) Pfeifer, M. A.; Williams, G. J.; Vartanyants, I. A.; Harder, R.; Robinson, I. K. Three-dimensional mapping of a deformation field inside a nanocrystal. *Nature* **2006**, *442*, 63–66, DOI: 10.1038/nature04867.
- (2) Robinson, I.; Harder, R. Coherent X-ray diffraction imaging of strain at the nanoscale. *Nature Materials* **2009**, *8*, 291–298, DOI: 10.1038/nmat2400.
- (3) Newton, M. C.; Leake, S. J.; Harder, R.; Robinson, I. K. Three-dimensional imaging of strain in a single ZnO nanorod. *Nat. Mater.* **2010**, *9*, 120–124, DOI: 10.1038/nmat2607.
- (4) Robinson, I. K.; Vartanyants, I. A.; Williams, G. J.; Pfeifer, M. A.; Pitney, J. A. Reconstruction of the Shapes of Gold Nanocrystals Using Coherent X-Ray Diffraction. *Physical Review Letters* **2001**, *87*, 195505, DOI: 10.1103/PhysRevLett.87.195505.
- (5) Schüllli, T. U.; Leake, S. J. X-ray nanobeam diffraction imaging of materials. *Current Opinion in Solid State and Materials Science* **2018**, *22*, 188–201, DOI: 10.1016/j.cossms.2018.09.003.
- (6) Yang, W.; Huang, X.; Harder, R.; Clark, J. N.; Robinson, I. K.; Mao, H.-k. Coherent diffraction imaging of nanoscale strain evolution in a single crystal under high pressure. *Nature Communications* **2013**, *4*, DOI: 10.1038/ncomms2661.

- (7) Ulvestad, A.; Sasikumar, K.; Kim, J. W.; Harder, R.; Maxey, E.; Clark, J. N.; Narayanan, B.; Deshmukh, S. A.; Ferrier, N.; Mulvaney, P.; Sankaranarayanan, S. K. R. S.; Shpyrko, O. G. *In Situ* 3D Imaging of Catalysis Induced Strain in Gold Nanoparticles. *The Journal of Physical Chemistry Letters* **2016**, *7*, 3008–3013, DOI: 10.1021/acs.jpcllett.6b01038.
- (8) Kim, D.; Chung, M.; Carnis, J.; Kim, S.; Yun, K.; Kang, J.; Cha, W.; Cherukara, M. J.; Maxey, E.; Harder, R.; Sasikumar, K.; K. R. S. Sankaranarayanan, S.; Zozulya, A.; Sprung, M.; Riu, D.; Kim, H. Active site localization of methane oxidation on Pt nanocrystals. *Nature Communications* **2018**, *9*, 3422, DOI: 10.1038/s41467-018-05464-2.
- (9) Carnis, J.; Kshirsagar, A. R.; Wu, L.; Dupraz, M.; Labat, S.; Texier, M.; Favre, L.; Gao, L.; Oropeza, F. E.; Gazit, N.; Almog, E.; Campos, A.; Micha, J.-S.; Hensen, E. J. M.; Leake, S. J.; Schüllli, T. U.; Rabkin, E.; Thomas, O.; Poloni, R.; Hofmann, J. P.; Richard, M.-I. Twin boundary migration in an individual platinum nanocrystal during catalytic CO oxidation. *Nature Communications* **2021**, *12*, DOI: 10.1038/s41467-021-25625-0.
- (10) Ulvestad, A.; Singer, A.; Cho, H.-M.; Clark, J. N.; Harder, R.; Maser, J.; Meng, Y. S.; Shpyrko, O. G. Single Particle Nanomechanics in *operando* Batteries via Lensless Strain Mapping. *Nano Letters* **2014**, *14*, 5123–5127, DOI: 10.1021/nl501858u.
- (11) Ulvestad, A.; Clark, J. N.; Singer, A.; Vine, D.; Cho, H. M.; Harder, R.; Meng, Y. S.; Shpyrko, O. G. In situ strain evolution during a disconnection event in a battery nanoparticle. *Physical Chemistry Chemical Physics* **2015**, *17*, 10551–10555, DOI: 10.1039/C5CP00372E.
- (12) Robinson, I. K. Optimisation of coherent X-ray diffraction imaging at ultrabright syn-

- chrotron sources. *Zeitschrift für Kristallographie Supplements* **2009**, *2008*, 27–35, DOI: <https://doi.org/10.1524/9783486992564-005>.
- (13) Leake, S.; Newton, M.; Harder, R.; Robinson, I. Longitudinal coherence function in X-ray imaging of crystals. *Opt. Express* **2009**, *17*, 15853–15859, DOI: <https://doi.org/10.1364/OE.17.015853>.
- (14) Raimondi, P. ESRF-EBS: The Extremely Brilliant Source Project. *Synchrotron Radiation News* **2016**, *29*, 8–15, DOI: [10.1080/08940886.2016.1244462](https://doi.org/10.1080/08940886.2016.1244462).
- (15) Martensson, N.; Eriksson, M. The saga of MAX IV, the first multi-bend achromat synchrotron light source. *Nuclear Instruments and Methods in Physics Research Section A: Accelerators, Spectrometers, Detectors and Associated Equipment* **2018**, *907*, 97 – 104, DOI: <https://doi.org/10.1016/j.nima.2018.03.018>, Advances in Instrumentation and Experimental Methods (Special Issue in Honour of Kai Siegbahn).
- (16) Singer, A.; Vartanyants, I. A. Coherence properties of focused X-ray beams at high-brilliance synchrotron sources. *J. Synch. Rad.* **2013**, 5–15, DOI: <https://doi.org/10.1107/S1600577513023850>.
- (17) Rack, A.; Scheel, M.; Hardy, L.; Curfs, C.; Bonnin, A.; Reichert, H. Exploiting coherence for real-time studies by single-bunch imaging. *Journal of Synchrotron Radiation* **2014**, *21*, 815–818, DOI: [10.1107/S1600577514005852](https://doi.org/10.1107/S1600577514005852).
- (18) Hettel, R. DLSR design and plans: an international overview. *Journal of Synchrotron Radiation* **2014**, *21*, 843–855, DOI: [10.1107/S1600577514011515](https://doi.org/10.1107/S1600577514011515).
- (19) Kim, J. W.; Ulvestad, A.; Manna, S.; Harder, R.; Fohtung, E.; Singer, A.; Boucheron, L.; Fullerton, E. E.; Shpyrko, O. G. Observation of x-ray radiation pressure effects on nanocrystals. *Journal of Applied Physics* **2016**, *120*, 163102, DOI: [10.1063/1.4965728](https://doi.org/10.1063/1.4965728).

- (20) Björling, A.; Carbone, D.; Sarabia, F. J.; Hammarberg, S.; Feliu, J. M.; Solla-Gullón, J. Coherent Bragg imaging of 60nm Au nanoparticles under electrochemical control at the NanoMAX beamline. *Journal of Synchrotron Radiation* **2019**, *26*, 1830–1834, DOI: 10.1107/S1600577519010385.
- (21) Huang, X.; Yang, W.; Harder, R.; Sun, Y.; Lu, M.; Chu, Y. S.; Robinson, I. K.; Mao, H.-k. Deformation Twinning of a Silver Nanocrystal under High Pressure. *Nano Letters* **2015**, *15*, 7644–7649, DOI: 10.1021/acs.nanolett.5b03568, PMID: 26484941.
- (22) Kolle Christensen, C.; Aaskov Karlsen, M.; Østergaard Drejer, A.; Pilgaard Andersen, B.; Lund Jakobsen, C.; Johansen, M.; Risskov Sørensen, D.; Kantor, I.; Ry Vogel Jørgensen, M.; Ravnsbæk, D. B. *Beam damage in operando X-ray diffraction studies of Li-ion batteries*; preprint, 2022; DOI: 10.26434/chemrxiv-2022-r1f7k.
- (23) Dupraz, M.; Leake, S. J.; Richard, M.-I. Bragg coherent imaging of nanoprecipitates: role of superstructure reflections. *Journal of Applied Crystallography* **2020**, *53*, 1353–1369, DOI: 10.1107/S1600576720011358.
- (24) Shabalin, A. G.; Yefanov, O. M.; Nosik, V. L.; Bushuev, V. A.; Vartanyants, I. A. Dynamical effects in Bragg coherent x-ray diffraction imaging of finite crystals. *Physical Review B* **2017**, *96*, 064111, DOI: 10.1103/PhysRevB.96.064111.
- (25) Newton, M. C.; Leake, S. J.; Harder, R.; Robinson, I. K. Three-dimensional imaging of strain in a single ZnO nanorod. *Nature Mat.* **2010**, *9*, 120–124, DOI: <https://doi.org/10.1038/nmat2607>.
- (26) Hofmann, F.; Phillips, N. W.; Harder, R. J.; Liu, W.; Clark, J. N.; Robinson, I. K.; Abbey, B. Micro-beam Laue alignment of multi-reflection Bragg coherent diffraction imaging measurements. *J. Synch. Rad.* **2017**, 1048–1055, DOI: <https://doi.org/10.1107/S1600577517009183>.

- (27) Maddali, S.; Allain, M.; Cha, W.; Harder, R.; Park, J.-S.; Kenesei, P.; Almer, J.; Nashed, Y.; Hruszkewycz, S. O. Phase retrieval for Bragg coherent diffraction imaging at high x-ray energies. *Physical Review A* **2019**, *99*, 053838, DOI: 10.1103/PhysRevA.99.053838.
- (28) da Silva, J. C.; Guilloud, C.; Hignette, O.; Jarnias, C.; Ponchut, C.; Ruat, M.; Labiche, J.-C.; Pacureanu, A.; Yang, Y.; Salome, M.; Bohic, S.; Cloetens, P. Overcoming the challenges of high-energy X-ray ptychography. *Journal of Synchrotron Radiation* **2019**, *26*, 1751–1762, DOI: 10.1107/S1600577519006301.
- (29) Pennicard, D.; Graafsma, H. Simulated performance of high-Z detectors with Medipix3 readout. *Journal of Instrumentation* **2011**, *6*, P06007–P06007, DOI: 10.1088/1748-0221/6/06/p06007.
- (30) Ponchut, C.; Cotte, M.; Lozinskaya, A.; Zarubin, A.; Tolbanov, O.; Tyazhev, A. Characterisation of GaAs:Cr pixel sensors coupled to Timepix chips in view of synchrotron applications. *Journal of Instrumentation* **2017**, *12*, C12023–C12023, DOI: 10.1088/1748-0221/12/12/c12023.
- (31) Maddali, S.; Park, J.-S.; Sharma, H.; Shastri, S.; Kenesei, P.; Almer, J.; Harder, R.; Highland, M. J.; Nashed, Y.; Hruszkewycz, S. O. High-Energy Coherent X-Ray Diffraction Microscopy of Polycrystal Grains: Steps Toward a Multiscale Approach. *Physical Review Applied* **2020**, *14*, 024085, DOI: 10.1103/PhysRevApplied.14.024085.
- (32) Carnis, J.; Gao, L.; Labat, S.; Kim, Y. Y.; Hofmann, J. P.; Leake, S. J.; Schüllli, T. U.; Hensen, E. J. M.; Thomas, O.; Richard, M.-I. Towards a quantitative determination of strain in Bragg Coherent X-ray Diffraction Imaging: artefacts and sign convention in reconstructions. *Scientific Reports* **2019**, *9*, 17357, DOI: 10.1038/s41598-019-53774-2.
- (33) Favre-Nicolin, V.; Girard, G.; Leake, S.; Carnis, J.; Chushkin, Y.; Kieffer, J.; Paleo, P.; Richard, M.-I. PyNX: high-performance computing toolkit for coherent X-ray imaging

- based on operators. *Journal of Applied Crystallography* **2020**, *53*, 1404–1413, DOI: 10.1107/S1600576720010985.
- (34) Simonne, D.; Carnis, J.; Atlan, C.; Chatelier, C.; Favre-Nicolin, V.; Dupraz, M.; Leake, S. J.; Zatterin, E.; Resta, A.; Coati, A.; Richard, M. I. Gwaihir: Jupyter Notebook graphical user interface for Bragg coherent diffraction imaging. *Journal of Applied Crystallography* **2022**, *55*, 1045–1054, DOI: 10.1107/S1600576722005854.
- (35) Carnis, J.; Atlan, C.; Simonne, D.; Leake, S.; Dzhigaev, D.; Kishore, K.; Dupraz, M.; Richard, M.-I.; Bot, D.; Singaravelan, K. carnisj/bcdi: v0.2.3. 2022; <https://doi.org/10.5281/zenodo.5963911>.
- (36) Haag, S. T.; Richard, M.-I.; Favre-Nicolin, V.; Welzel, U.; Jeurgens, L. P.; Ravy, S.; Richter, G.; Mittemeijer, E. J.; Thomas, O. In situ coherent X-ray diffraction of isolated core–shell nanowires. *Thin Solid Films* **2013**, *530*, 113–119, DOI: 10.1016/j.tsf.2012.07.060.
- (37) Boller, K.; Haelbich, R. P.; Hogrefe, H.; Jark, W.; Kunz, C. Investigation of carbon contamination of mirror surfaces exposed to synchrotron radiation. *Nuclear Instruments and Methods in Physics Research* **1983**, *208*, 273–279, DOI: 10.1016/0167-5087(83)91134-1.
- (38) Chushkin, Y.; Zontone, F. Upsampling speckle patterns for coherent X-ray diffraction imaging. *Journal of Applied Crystallography* **2013**, *46*, 319–323, DOI: 10.1107/S0021889813003117.
- (39) Maddali, S.; Calvo-Almazan, I.; Almer, J.; Kenesei, P.; Park, J.-S.; Harder, R.; Nashed, Y.; Hruszkewycz, S. O. Sparse recovery of undersampled intensity patterns for coherent diffraction imaging at high X-ray energies. *Scientific Reports* **2018**, *8*, 4959, DOI: 10.1038/s41598-018-23040-y, Number: 1 Publisher: Nature Publishing Group.

- (40) Luke, D. R. Relaxed Averaged Alternating Reflections for Diffraction Imaging. *Inverse Probl.* **2004**, *21*, 37–50, DOI: 10.1088/0266-5611/21/1/004.
- (41) Fienup, J. R. Phase retrieval algorithms: a comparison. *Appl. Opt.* **1982**, *21*, 2758–2769, DOI: 10.1364/AO.21.002758.
- (42) Fienup, J. R. Reconstruction of a complex-valued object from the modulus of its Fourier transform using a support constraint. *J. Opt. Soc. Am. A* **1987**, *4*, 118–123, DOI: 10.1364/JOSAA.4.000118.
- (43) Fienup, J. R.; Wackerman, C. C. Phase-retrieval stagnation problems and solutions. *J. Opt. Soc. Am. A* **1986**, *3*, 1897–1907, DOI: 10.1364/JOSAA.3.001897.
- (44) Gerchberg, R.; Saxton, O. A Practical Algorithm for the Determination of the Phase from Image and Diffraction Plane Pictures. *Optik* **1972**, *35*, 237–246, DOI: <https://doi.org/10.1038/nmat2607>.
- (45) Fienup, J. R. Reconstruction of an object from the modulus of its Fourier transform. *Optics Letters* **1978**, *3*, 27–29, DOI: 10.1364/OL.3.000027.
- (46) Marchesini, S.; He, H.; Chapman, H. N.; Hau-Riege, S. P.; Noy, A.; Howells, M. R.; Weierstall, U.; Spence, J. C. H. X-Ray Image Reconstruction from a Diffraction Pattern Alone. *Phys. Rev. B* **2003**, *68*, 140101, DOI: 10.1103/PhysRevB.68.140101.
- (47) Clark, J. N.; Huang, X.; Harder, R.; Robinson, I. K. High-resolution three-dimensional partially coherent diffraction imaging. *Nature Communications* **2012**, *3*, 993, DOI: 10.1038/ncomms1994.
- (48) Favre-Nicolin, V.; Leake, S.; Chushkin, Y. Free Log-Likelihood as an Unbiased Metric for Coherent Diffraction Imaging. *Sci. Rep.* **2020**, *10*, 2664, DOI: <https://doi.org/10.1038/s41598-020-57561-2>.

## **Data availability**

When published the data will be uploaded to the CXI database: <https://www.cxidb.org>.

## **Code availability**

The code can be found here: <sup>33,35</sup>

## **Competing interests**

The authors declare no competing interests.